An equilibrium criterion for plastic debris fate in wave-driven transport

Claudio Iuppa [*], Giovanni Passalacqua , Carla Faraci

Department of Engineering, University of Messina, Contrada di Dio, Messina 98166, Italy

ABSTRACT

The nearshore zone turns out to be the area with the higher concentration of plastic debris and, for this reason, it is important to know the processes that affect the transport and the fate of this type of litter. This study focuses on investigating the dynamics of various plastic types under several hydrodynamic conditions primarily induced by waves. 2D tests were carried out at the Hydraulic Laboratory of the University of Messina reproducing the main phenomena that occurred during the wave propagation on a planar beach. More than 200 different conditions were tested changing the wave characteristics, the water depth, the plastic debris characteristics (density and shape), and the roughness of the fixed bottom. In general, it can be observed that the reduction in particle displacement occurs due to: i) a decrease in wave steepness; ii) an increase in depth; iii) an increase in particle size; iv) an increase in plastic density. However, the experimental investigation shows that some plastic characteristics and bed roughness, even when hydraulically smooth, can alter these results. The experimental data analysis identified a criterion for predicting the short-term fate of plastic debris under wave action. This criterion to determine equilibrium conditions, based on an empirical relationship, takes into account the wave characteristics, the bed roughness and slope, and the weight of the debris.

1. Introduction

In the last decades, huge amounts of plastic debris have been released into coastal seas, coming from densely populated or industrialized riverine and littoral areas, mainly through runoff. The items found in the oceans belong to several types of polymers, including polypropylene, polyethylene, nylon and many others (Uzun et al., 2022). Based on their size, plastics are commonly classified into macro (characteristic dimension larger than 25 mm), *meso* (25 down to 5 mm) micro (5 to 1 mm) mini-micro (1 mm to 1 μm) and nano (less than 1 μm) (Crawford and Quinn, 2017).

Once diffused in deep oceans, debris distribution is largely determined by ocean circulation, particularly waves and currents. Knowing how and where the sea transports the plastic is essential to understand its fate and impact on marine ecosystems. However, though plastic motion under the action of oceanic currents has been relatively well understood (Van Sebille et al., 2020), little is known as regards its transport in intermediate and shallow coastal waters, where nonlinear waves and wave-induced currents primarily control the hydrodynamics. In these zones, the transport processes are complex due to the superimposition of several phenomena such as wave breaking, wave asymmetry which generates steady streaming close to the bottom (Scandura

et al., 2012; Longuet-Higgins, 1953), the current generated by the waves (cross and long-shore), and the bed roughness which may alter the wave-current interaction along the column (Faraci et al., 2021).

Plastic waste released into the sea is therefore subject to the action of waves and currents which, depending on plastic buoyancy, shape and dimension, can drag it towards the beach or wash it offshore (Forsberg et al., 2020). The debris interaction with the hydrodynamic forcings has been studied both numerically and experimentally. Typically, even though not strictly, the large-scale ocean circulation, focusing on garbage patches and other floating structures, is mainly explored by numerical studies while laboratory investigations are almost preferred to tackle plastic litter interaction with beaches and seabeds (Hardesty et al., 2017; Passalacqua et al., 2023).

An overview of existing numerical models specifically focusing on floating marine litter has been provided by Hardesty et al. (Hardesty et al., 2017), who identified several unresolved research questions, specifically addressing the importance of properly identifying the sources of marine plastic. Among these studies, Lebreton et al. (Lebreton et al., 2012), coupled a global ocean circulation model with a Lagrangian particle tracking method to reproduce waste transport and accumulation in the major ocean basins over a 30-year timespan. They predicted the largest debris concentration in the northern hemisphere, particularly over the North Atlantic and Pacific Oceans, as a

Nomenclature

Acronyms

EVA	Ethylene Vinyl Acetate
Ny	Nylon
PET	Polyethylene terephthalate

Physics quantities and coefficients

α	Bed slope
$\alpha_{g,max}$	Slope at $X_{g,max}$
δ	Thickness of the boundary layer
γ_f	Friction coefficient
γ_s	Corrective factor
ν	Water viscosity
$\overline{U_m}$	Maximum values of Longuet-Higgins steady streaming
$\overline{u_m}$	Maximum values of the phase-average velocity
$\overline{U}$	Longuet-Higgins steady streaming
ρ_s	Density of plastic
ρ_w	Density of water
τ	Bed shear stress
Θ_p	Threshold parameter of plastic transport
Θ_s	Shields threshold parameter
ξ	Iribarren number
a	Incident wave amplitude
a_p, b_p, c_p	Longest, intermediate, and shortest particle axis respectively
A_w	Near-bottom semi-orbital excursion
C_D	Drag coefficient of the plastic particle
csf	Corey shape factor
d_D	Equivalent diameter of a sphere with the same settling velocity
D_n	Diameter of a volume-equivalent sphere
d_p	Characteristic length of the plastic particle
f_w	Friction factor
g	Gravitational acceleration
H	Incident wave height
$h_{g,max}$	Depth at $X_{g,max}$
k_0	Wave number at deep water
k_r	Reflection coefficient
k_s	Shoaling coefficient
k_w	Wave number at Vectrino measurement points
$k_{g,max}$	Wave number estimated at equilibrium point
L	Shallow-water wave length
L_0	Wavelength at deep water
n_z	Number of zones
P_p	Parameter used as a measure of the propensity of the particles to drift
RE	Reynolds number
Re_p	Reynolds number of the plastic particle
s	Relative density of the plastic
T	Wave period
t_i	Residence time of the centroid
u_*	Friction velocity
u_w	Near-bottom velocity
u_{ov}	Wave orbital velocity just above the bottom
w_s	Settling velocity of the plastic particle
X'_g	Position of the global centroid weighted as a function of the residence time
$X_{g,max}$	Drift component of $X_{g,s}$ at equilibrium point
$X_{g,s}$	Displacement of centre of masses of the whole sample of plastic
X_g	Drift component of $X_{g,s}$
$X^*_{g,max}$	Maximum distance covered by the centroid ($X_{g,max}$) normalized by the incident wave height

consequence of more intense economic activities and higher population.

Moving to smaller scales and confined basins, Liubartseva et al. (Liubartseva et al., 2018) attempted to simulate pathways and fate of plastic litter released into the Mediterranean Sea under the effect of waves and currents as predicted by a hydrodynamic-wave modelling system. They found that coastline plastic pollution is mainly caused by terrestrial sources of plastics, identifying the most contaminated areas in the proximity of the plastic debris sources. Similar results were also obtained by Guerrini et al. (Guerrini et al., 2021) by applying particle tracking to map microplastic diffusion at a Mediterranean scale. Jalón-Rojas et al. (Jalón-Rojas et al., 2019) developed a 3D particle tracking model able to include both particle setting and vertical current to predict the debris movement within the water column. The model also simulates several phenomena that can occur when plastics are dispersed in an aquatic environment. In particular, it evaluates the effects of wind transport, beaching, washing-off, degradation, aggregation and biofouling formation. The model has been applied to several case studies, including those recently conducted by Elisei Schicchi et al. (Elisei Schicchi et al., 2023) in the Río de la Plata (Argentina), Liao et al. (Liao et al., 2023) in the south-eastern side of Australia and Stagnitti and Musumeci (Stagnitti and Musumeci, 2024) in the north side of Sicily. Similarly, Pilechi et al. (Pilechi et al., 2022) set a numerical framework to predict microplastic fate and transport in enclosed basins and coastal waters, able to account for both positively and negatively buoyant particles, as well as biofouling and degradation processes, validating it with a case study located in eastern Canada.

From this quick overview, it is clear that numerical models can provide insights regarding the general circulation and diffusion processes at a basin or sub-basin scale, but they do not face the mechanisms that lead plastic debris to be mobilized by means of a physical-based approach, transported and beached or washed off by the wave action. Indeed, generally, most of these processes are modelled by empirical relationships or probabilistic models (Jalón-Rojas et al., 2019). On the contrary, an interpretation of such processes can be attempted via physical modelling.

Similarly to sediment transport, in the case of plastics, experimental research focuses on studying certain characteristic phenomena. In particular, experimental efforts have been particularly devoted to study: settling velocities of plastic samples (Francalanci et al., 2021; Yu et al., 2022; Goral et al., 2023a), incipient motion (Yu et al., 2022; Waldschläger and Schüttrumpf, 2019; Goral et al., 2023b), wave-induced distribution of debris in the coastal zone (Forsberg et al., 2020; Alsina et al., 2020; Núñez et al., 2023) or the interaction of particles with sediments laying on the seabed (Kerpen et al., 2020; Guler et al., 2022; Larsen et al., 2023). More specifically, Francalanci et al. (Francalanci et al., 2021) propose a comprehensive approach to interpret the fall velocity of particles with several shapes in different hydraulic regimes from laminar to turbulent, testing most of the existing formulations valid for natural sediments on a specifically acquired dataset and suggesting a modified, geometrically based, equivalent diameter. Yu et al. (Yu et al., 2022) highlighted the importance of focusing on the drag coefficient, resulting from the balance of gravity, buoyancy and drag forces. They proposed a new formula for predicting drag coefficient accounting for both the particle sphericity and the Corey shape factor. Goral et al. (Goral et al., 2023a) further improved Yu et al. (Yu et al., 2022) formulation by including also physical justification of particle orientation during fall. Indeed, they observed that plastic samples tend to settle with the largest projection area orthogonal to the line

Table 1

Summary of studies on non-buoyant plastic debris transport due to waves and wind.

Reference	Main information on the test
Forsberg et al. (2020)	*Distribution in the nearshore zone due to wave and wind*
	Shapes: Pellet, fibre and sheet (6 samples)
	Size range: 1.68–5.44 mm
	Density range: 1040–1370 kg/m^3
	Number of hydrodynamics conditions: 4
	Typical test duration: 5 min
	Continuous monitoring: No
Kerpen et al. (2020)	*Distribution in the nearshore zone due to regular waves*
	Shapes: spherical and disk-shaped (13 samples)
	Size range: 0.5–4.1 mm
	Density range: 920–1983 kg/m^3
	Number of hydrodynamics conditions: 2
	Typical test duration: 23 h
	Continuous monitoring: No
Alsina et al. (2020)	*Cross-shore transport due to regular wave*
	Shapes: spherical (11 samples)
	Size range: 4–12 mm
	Density range: 760–1340 kg/m^3
	Number of hydrodynamics conditions: 4
	Typical test duration: 17 min
	Continuous monitoring: Yes
Guler et al. (2022)	*Distribution in the nearshore zone due to two different beach profiles*
	Shapes: cubes, spheres, disks (circular and square) and cylinders (square and rectangular) (18 samples)
	Size range: 2–8.7 mm
	Density range: 1062–1358 kg/m^3
	Number of hydrodynamics conditions: 3
	Typical test duration: 88 h
	Continuous monitoring: No
Núñez et al. (2023)	*Distribution in the nearshore zone due to regular and irregular waves*
	Shapes: 2D regular and irregular fragments (15 samples)
	Size range: 1.2–28.4 mm
	Density range: 380–1340 kg/m^3
	Number of hydrodynamics conditions: 3
	Typical test duration: 18 min
	Continuous monitoring: Yes

of motion, and accordingly they corrected the length scale used within the drag coefficient. In order to predict incipient motion, both Waldschläger and Schüttrumpf (Waldschläger and Schüttrumpf, 2019) and Yu et al. (Yu et al., 2022) proposed empirical expressions by studying the plastic particle motion on both smooth and sediment beds.

The proposed relationships are based on the characteristics of the plastic particles (geometry, density, etc.) and the sediment bed. Goral et al. (Goral et al., 2023b) highlights some limitations of applications for both methods. Studying the incipient motion conditions in a circular flume for several regular and irregular microplastic particle groups with various sizes and densities, they demonstrated that the Shields curve can also be applied in the case of plastics by adopting appropriate correction coefficients.

Studies on plastic transport generally analyse the behaviour of plastics at the scale of individual storm events. At the same way, the term *fate* should be interpreted as transport over a relatively short period. For this reason, this paper will refer to the term *short-term fate*.

Non-buoyant plastic transport in intermediate and shallow waters has been first dealt with by Forsberg et al. (Forsberg et al., 2020). They attempted to understand how different plastic litter samples distribute in the nearshore when subject to regular waves and a wind field. According to their results, the cross-shore distribution of plastic is controlled by both density and flow conditions. Basically, heavy samples tend to be entrapped within the breaking zone, while light ones are more likely to be beached unless offshore wind is present. However, the study lacks of generalisation as only one condition for waves and winds is considered. Kerpen et al. (Kerpen et al., 2020) studied the behaviour of several plastic samples with different sizes, shapes, and densities in a wave flume with a mobile bottom. Each kind of plastic was tested under the action of one regular wave. The authors found that accumulation peaks depend on the particle properties. In particular, the accumulation peaks

tend to move towards shallow water with increasing particle size or density. Alsina et al. (Alsina et al., 2020) studied plastic particle transport in intermediate water depth, testing plastic buoyant and non-buoyant spheres under the action of regular waves. The authors found that floating particles move in the wave propagation direction according to the so-called Stokes drift, with increasing velocities as the wave steepness increases; unlikely non-floating litter though moving shoreward, exhibits decreasing velocities as the wave steepness increases. Núñez et al. (Núñez et al., 2023) analysed a variety of plastic debris, randomly released on the run-up zone or uniformly distributed along the flume, under the action of two regular waves and an irregular one. In this way, the authors aimed on one side to analyse the input rate of plastic coming from land to the sea, and on the other to study the dispersion of the debris already present in the marine environment. In the first case, they found predominant accumulation in the breaking and nearshore zones, while in the second one, they observed that only steeper waves could transport the plastic debris from the offshore zone. Additionally, the more buoyant the plastic debris, the more likely it is to be trapped on the shoreline, while no relevant effects were found moving from regular to irregular waves. Guler et al. (Guler et al., 2022) studied the cross-shore distribution of non-buoyant plastic particles under irregular waves on live sediment-sloping beds. Several particle groups having various shapes, densities, and sizes were tested. The main finding was that the accumulation patterns largely depend on the particle characteristics (shape and weight) and on the initial bottom profile.

Table 1 summarises the main information about the studies on non-buoyant plastic debris transport.

The described experimental studies represent significant contributions to understanding the dynamics of plastics in coastal areas as well as the field activities. Indeed, there are several studies that analyse the concentration of plastics on beaches. For example, De-la Torre et al. (De-

la Torre et al., 2020) and Li et al. (Li et al., 2023), who studied the distribution of microplastics in various zones, demonstrated high variability in plastic abundance seasonally but also among adjacent beaches. Field and experimental data can also be used as benchmarks for the validation of numerical models. However, the experimental research activities lack the definition of a generalized approach that allows to consider, for example, the non-linearities associated with hydrodynamics variability on the fate of plastics. As seen in Table 1, the different experimental campaigns show a limited variability of the hydrodynamic conditions. Moreover, detailed analyses of the local hydrodynamic conditions that can influence the transport process and the interaction of the bed with the plastics are generally absent. To overcome this gap, the present study focused on non-floating plastics and their interaction with the bottom slope. Examining various plastic types, different bottoms, and several hydrodynamic conditions mainly related to the waves enabled the identification of a relationship between the stabilising and destabilising forces acting on plastic debris. In particular, the identified approach evaluates for a group of particles arranged on the seabed whether the hydrodynamic forcing can overcome the resistances induced by the bed (roughness and slope) and the weight of the particles. In this perspective, more than 200 different conditions were tested at the Hydraulic Laboratory of the University of Messina changing the wave characteristics, water depth, plastic debris characteristics (density and shape), and the roughness of the fixed bottom.

This paper is structured as follows. The next section describes the experimental campaign detailing the tools and methodologies used to estimate the quantities necessary to pursue the research objectives. Section 3 describes the analyses of the experimental results focusing on the study of the wave flow close to the bottom and on the dynamics of plastics in water, driven by both their weight and the waves. In particular, section 3.1 describes the water velocity close to the bottom, specifically the generation of a near-bed current by the waves, which influences the dynamics of plastic debris. Section 3.2 describes the settling velocity of the tested samples. The investigation of particle resistance offered during its sedimentation helped in justifying certain behaviours observed during wave-induced transport. Section 3.3 focuses on the transport process of plastics. Comparative analyses highlighted the impacts associated with characteristics of wave, plastic and bed. In section 3.4, a relationship is proposed to predict whether plastic particles will be transported to the breaking zone or if their movement will be hindered by bed effects. The paper ends with some concluding notes.

2. Experimental setup, instrumentation and procedure

2.1. Laboratory equipment

To study the dynamics of plastic particles in the coastal zone subject to wave motion, a model of a beach profile with a variable slope was constructed inside an 18.5 m long wave channel. The flume has a rectangular cross-section of 0.4 m × 0.8 m and is equipped with a flap-type wave maker and an absorption chamber (see Fig. 1a).

The beach profile, starting about 8 m from the wave maker, was made of steel panels. To simulate the gradual decrease of the depth, an initial sloping section of 20 % precedes a flat section and a final section having initially a variable slope (part A) and then a constant slope of 20 % (part B) (see Fig. 1b). In particular, part A was designed to have a gradually varying slope to smooth the transition from the flat section to the section with a 20 % slope. Approximately 1 m of the bottom surface extending from the beginning of part A to the shoreline is covered with interchangeable aluminium panels with controlled roughness. Two types of surfaces were used to study the behaviour of plastic particles for different roughness conditions: a smooth and a rough one, the latter made of sand grains with diameter $d_{50} = 1.4$ mm glued on the panel. A video camera with a resolution of 1920 × 1080 pixels, 30× zoom (4 K), 28.8 mm wide angle lens, and a frame rate of 25 fps was placed at a height of 1 m to record the tests, framing both the plastic sample input point and the shoreline from above. Part A and approximately the first meter of part B of the slope, up to the shoreline, are recorded by the camera. Measurement of the height of the free surface was made by four-wave gauges placed along the flume. The first one was placed near the wave maker while the other three were placed near the beach profile and were used to calculate the reflection coefficient with the method of Mansard and Funke (Mansard and Funke, 1980). For the characterization of the flow field, fluid velocities were measured through a Vectrino Profiler (Nortek As.). This device, consisting of four beams allows measurement of velocities along three directions, namely the direction of wave propagation, the one orthogonal to it and vertically.

It must be pointed out that velocity measurements and plastic transport measurements were performed separately in two different stages, thus the same hydrodynamic conditions were generated twice, once for acquiring the flow field and the other for studying the mobility of the plastic samples.
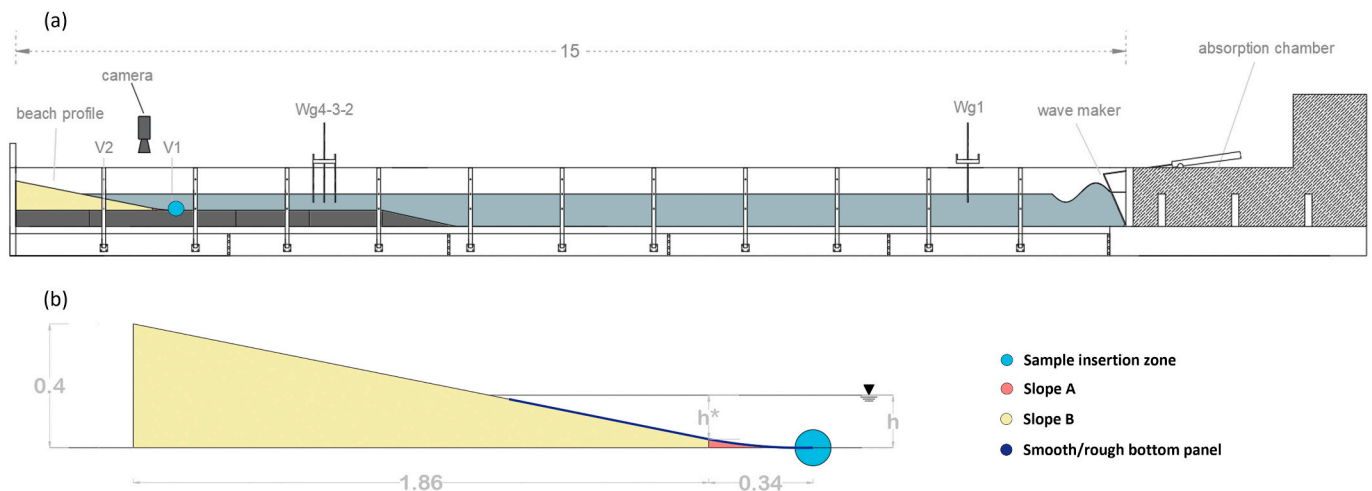

Fig. 1. Wave flume: a) longitudinal cross-section of the wave flume used in the experimental campaign; b) cross-section of the beach profile used in the experiments. The symbol Wg indicates the wave gauges placed along the flume. The symbol V indicates the positions of the Vectrino Profiler (Nortek As.). The initial slope of the submerged beach (part A) was designed to have a gradually varying slope. The part B is characterised by a constant slope equal to 20 %. The thick blue line on the slope indicates the area with controlled roughness. Distances are expressed in meters. (For interpretation of the references to colour in this figure legend, the reader is referred to the web version of this article.)

Table 2

The simulated range conditions for the performed runs are shown: water depth at the initial point (h), wave period (T), shallow-water wave length (L), incident wave height (H), the reflection coefficient (k_r) and the Iribarren number (ξ).

h [cm]	T [s]	L [cm]	H [cm]	k_r	ξ
23	$1.00 - 1.66$	$127.3 - 235.5$	$1.5 - 6.4$	$0.15 - 0.57$	$0.63 - 2.52$
18	$1.00 - 1.66$	$117.2 - 210.9$	$1.8 - 9.8$	$0.18 - 0.59$	$0.69 - 2.14$
15	$1.00 - 1.66$	$109.4 - 195.6$	$2.1 - 8.4$	$0.15 - 0.46$	$0.72 - 1.95$

Table 3

Characterization of the used samples: id indicates the sample name, ρ_s indicates the density of the plastic, a_p, b_p and c_p are the longest, intermediate, and shortest particle axis respectively, *csf* the Corey shape factor and D_n is the diameter of a volume-equivalent sphere.

Plastic	id	ρ_s [g/cm³]	a_p [mm]	b_p [mm]	c_p [mm]	csf	D_n [mm]
PET	PET-01	1.373	10.50	5.00	0.12	0.015	2.29
PET	PET-02	1.373	5.00	5.00	0.12	0.022	1.79
Nylon	Ny-01	1.146	10.50	5.00	0.80	0.154	4.31
Nylon	Ny-02	1.146	5.00	5.00	0.80	0.217	3.38
EVA	EVA-01	1.010	14.00	6.00	6.00	0.643	9.22
EVA	EVA-01	1.010	7.00	6.00	6.00	0.926	7.23

2.2. Hydrodynamic condition

To study the dynamics of plastics, the characteristics of the simulated waves were varied. Each run lasted up to 120 s, the time needed to mobilize the samples and reach their ultimate condition.

Three different water depth conditions were considered at the beach toe: 0.23 m, 0.18 m and 0.15 m. Six different wave conditions were tested for each depth by varying the period and amplitude of the wave maker. The values of incident wave height H and of reflection coefficient were calculated through the 3-gauges method (Mansard and Funke, 1980), while the wavelength L was estimated with the dispersion relation. For each configuration was also estimated the Iribarren number which is a nondimensional parameter useful for the classification of the studied beach:

$$\xi = \frac{tan\alpha}{\sqrt{(H/L)}} \tag{1}$$

where α is the beach slope. The beach studied in the experimental campaign is reflective since the Iribarren number is larger than 0.3.

Table 2 shows the simulated wave conditions.

2.3. Characteristics of plastic particles and method for tracking applied

The following types of plastic were considered in the experimental campaign: polyethylene terephthalate (PET), nylon and ethylene vinyl acetate (EVA). For each type of plastic two different shapes were used. In total six different samples were investigated. Table 3 shows the main characteristics of the analysed samples. ρ_s indicates the density of the plastic, a_p, b_p and c_p are the longest, intermediate, and shortest particle axis respectively, *csf* the Corey shape factor and D_n is the diameter of a volume-equivalent sphere. The shape of the plastic debris can be classified as follows: PET-01 and Ny-01 are rectangular prisms; PET-02 and Ny-01 are square prisms; EVA-01 and EVA-02 are cylinders.

Each sample, made of 100 particles, was located at the beach toe at the beginning of each test (see Fig. 1). The tracking of the plastic particles, mobilized by the action of the wave motion, was performed by means of a post-processing analysis of the images acquired through a video camera. The video camera was positioned as indicated in Fig. 1 and allowed for the monitoring of the sample's evolution over time from above and enabled the tracking of their movements through the application of blob analysis. The main steps performed on each video are as follows: i) division of the video into frames; ii) spatial transformation of frames; iii) transformation of frames from RGB image to binary image; iv) application of blob analysis; v) application of filter to the signal to eliminate noise. Blob analysis is a computer vision technique for detecting the connected pixels in an image that differ in characteristics and properties from surrounding pixels (Moeslund, 2012).

For each frame, the coordinates of the global centroid, i.e. the centre of masses of the whole sample, were estimated ($X_{g,s}$). For further details about the frame analysis and the method to estimate $X_{g,s}$ please refer to Passalacqua et al. (Passalacqua et al., 2023). Fig. 2 shows an example of the evolution of $X_{g,s}$ over time estimated using the described method. The oscillating and drift components of the centroid displacement were derived from the original signal of $X_{g,s}$. Given the aim of the current study, the analysis was specifically directed towards the drift only component, denoted hereafter by the symbol X_g. At the equilibrium point, when the drift component X_g assumes a constant value, the maximum values of the drift component, depth, and slope are denoted by the symbols $X_{g,max}$, $h_{g,max}$, and $\alpha_{g,max}$, respectively.

2.4. Dimensional analysis

The displacement of the debris sample X_g in the considered time t may expressed by the generic function F:

$$\frac{\Delta X_g}{\Delta t} = \mathbf{F}(F_w, F_p, F_b) \tag{2}$$

where F_w indicates a group of quantities related to the hydrodynamic conditions; F_p indicates a group of quantities related to the plastic characteristics and F_b indicates a group of quantities related to the bed characteristics. In the context of this study, we are interested in identifying the equilibrium condition, i.e. when the forcing is unable to transport the particles. In this case $\frac{\Delta X_g}{\Delta t}$ is equal to 0. Therefore, it is possible to identify a relationship between the stabilising and destabilising forces.

The analysis of the results has revealed that the investigated process is highly complex and characterised by several non-linearities. However, after thorough analysis, it was possible to uniquely characterize the studied tests through a function G of the following quantities:

$$\Theta_p = \mathbf{G}(F_w, F_p, F_b) = \mathbf{G}(g, \overline{u}, \rho_w, \rho_p, D_n, \alpha, \gamma_f) \tag{3}$$

where Θ_p is a threshold parameter of plastic transport, g is the gravitational acceleration, $\overline{u}$ is a characteristic velocity of water due to wave, ρ_w is the water density, ρ_p is the particle density, D_n is a characteristic size of the plastic particles, α is the bed slope, and γ_f is a friction coefficient.

3. Experimental results

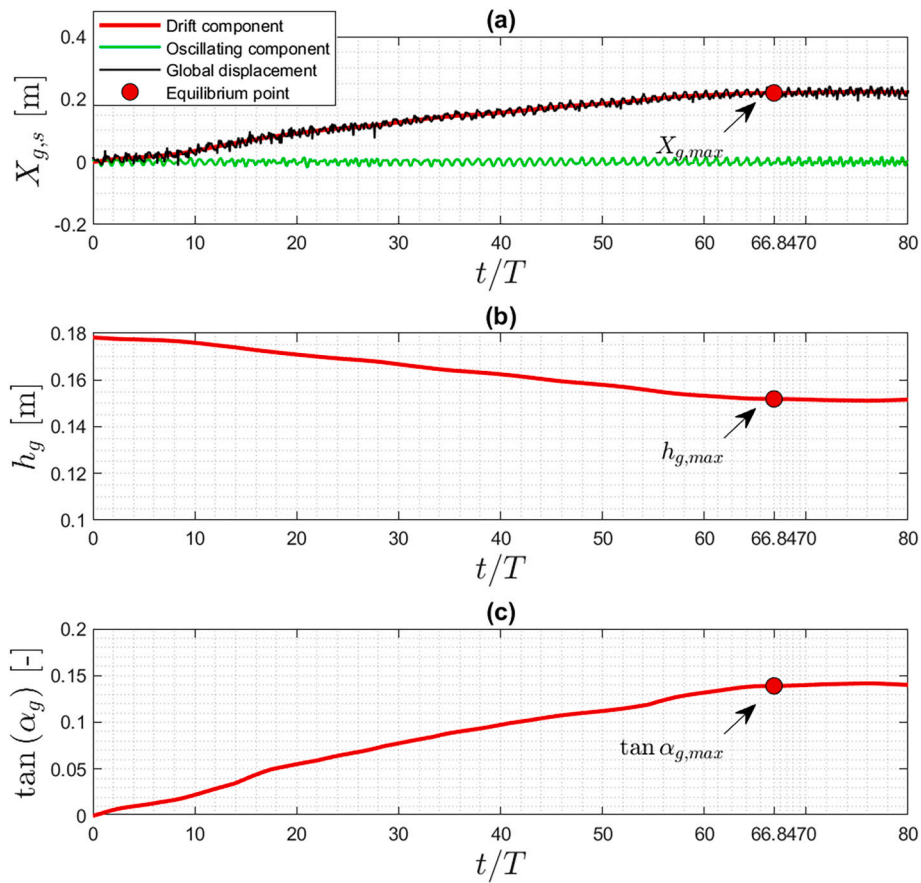In the following sections, the identified quantities and their impact

Fig. 2. Example of the evolution of $X_{g,s}$ over time. a) $X_{g,s}$ oscillating and drift components of the centroid displacement; b) water depth at the centroid position; c) bed slope at the centroid position. The data refer to sample Ny-01 under the following hydrodynamics conditions: H = 9.77 cm, $T = 1$ s and h = 18 cm. The test was carried out using the smooth bottom. The equilibrium point is reached at 67 T. From this instant, the advances of the sample are compensated by retreats. At the equilibrium point, the values of the drift component, the depth and the slope are indicated $X_{g,max}$, $h_{g,max}$ and $\alpha_{g,max}$ respectively.
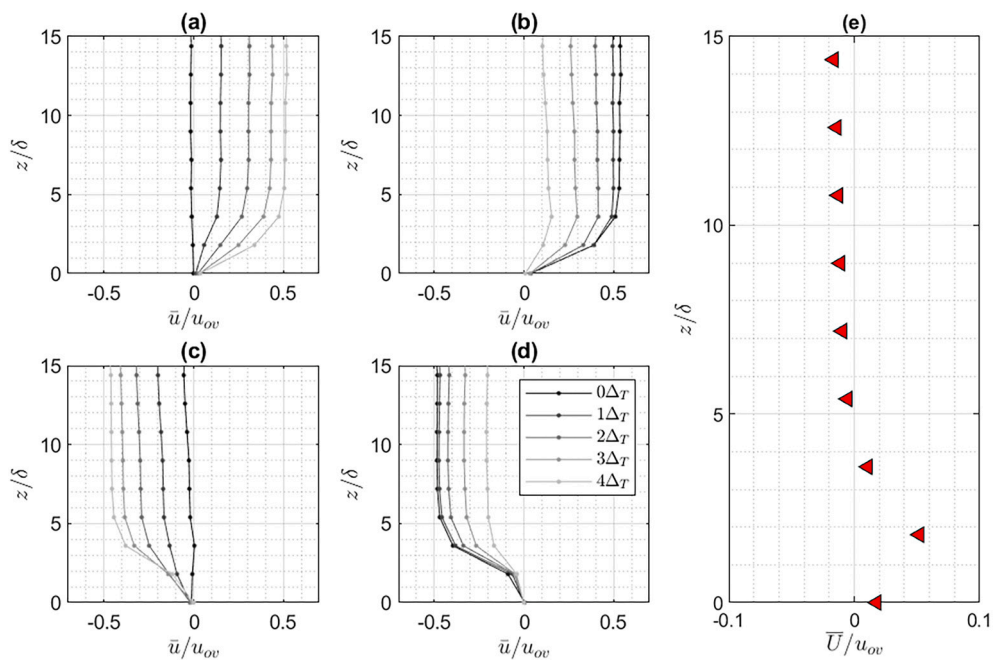
Fig. 3. Comparison between the phase-averaged velocity profiles measured the rough surfaces at position V1. The data refer to the test with the following hydrodynamics conditions: H=10.3 cm, T=1 s and h=18 cm. δ and u_{ov} are equal to 0.06 cm and 0.40 m/s respectively. The value of Δ_T was set equal to 0.05T. a) mean velocity profiles for the phases between 0T and 0.20T; b) between 0.25T and 0.45T; c) between 0.50T and 0.70T; d) between 0.75T and 0.95T; e) time averaged velocity profile.

on the transport process will be analysed. In particular, the analysis focuses on: i) the water velocity close to the bottom; ii) the settling velocity of the tested samples; iii) the transport process of plastics.

3.1. Water velocity close to the bottom

The time average of a fluctuating flow often results in a nonzero mean (Riley, 2001). As a consequence, in the case of gravity waves, in addition to the predominant oscillating motion, it is possible to observe a second-order velocity known as Stokes drift (Longuet-Higgins, 1953; Stokes, 1847). The Stokes drift is always directed as the direction of the wave propagation. This occurs for two main reasons (Fredsoe and Deigaard, 1992): *i*) the amplitudes of the positive phases are greater the those negative; *ii*) at the top of the elliptic displacement of the particle, the velocity is higher than at the bottom. Inside a wave flume, as in the case under consideration, the water transported by the Stokes drift is compensated by the generation of a return flow known as undertow current. Among such currents, a third current (Longuet-Higgins streaming) close to the bottom exists which has high physical importance in either the sediment or the non-buoyant plastic debris transport. Longuet-Higgins (Longuet-Higgins, 1953) indeed demonstrated for the first time the existence of steady streaming in the boundary layer which persists at the outer edge of the boundary layer. The author showed that the steady streaming has the same direction as incident waves for the laminar oscillatory boundary layer.

Fig. 3 (a to d) compares different phase-averaged velocity profiles measured at position V1 (see Fig. 1) in the present experimental campaign with rough bed.

The velocity was made dimensionless using the amplitude of the wave orbital velocity just above the bottom due to a monochromatic wave:

$$u_{ov} = \frac{\pi H}{T sinh(k_0 h)} \tag{4}$$

where k_0 is the wave number estimated by applying the dispersion relationship for deep water (wavelength is equal to $L_0 = \frac{2\pi}{k_0}$). The water depth was made dimensionless using the theoretical thickness of the boundary layer in laminar conditions ($\delta = \sqrt{\frac{\nu T}{\pi}}$, where ν is the water viscosity).

The velocity profile over the smooth bed, though acquired, is not shown because it was observed that a smooth bed distorts the reflected acoustic signal causing generally an underestimation of the velocity for the negative phases (Thomas et al., 2017). However, since the two beds can be considered hydraulically smooth, the velocity profile is expected to be similar between the two tests under similar hydrodynamics conditions. According to Collins (Collins, 1963), the bottom boundary layer observed for both surfaces was laminar since the values of $u_{ov}\delta/\nu$ are below 160.

The comparison between the positive and negative phases of the velocity reveals a noticeable asymmetry in the velocity signal, which is responsible for the generation of the Longuet-Higgins streaming velocity. Fig. 3(e) shows the average velocity profile for the same test. The obtained velocities, averaged on all wave periods ($\overline{U}$), correspond to the Longuet-Higgins steady streaming. The positive values indicate that the streaming has the same direction as incident waves.

Fig. 4a) shows the maximum values of the phase-average velocity profile for the rough bed case($\overline{u_m}$), made dimensionless through the wave celerity as a function of the wave steepness $k_w a$. The symbols k_w and a indicate the wave number estimated by applying the dispersion relationship using the water depth at V1 and V2 and the incident wave amplitude ($a = H/2$) respectively. Conversely, Fig. 4b) shows the maximum values of the time-averaged velocity ($\overline{U_m}$) made dimensionless also in this case through the wave celerity, for the same bed. The data refers to measurements acquired at both the position V1 and V2.

As seen from the analysis of Fig. 4, the increase in wave steepness determines an increase in the maximum values of the phase-average velocity and the bottom flow. A further aspect is that the parameters $\frac{\overline{u_m}T}{L_0}$ and $\frac{\overline{U_m}T}{L_0}$ exhibit similar behaviours at the two measurement points (V1 and V2). The two prediction relationships defined for the two dimensionless velocities are shown in Appendix A.

It can be observed that the maximum ratio between the plastic debris thickness c_p and δ (considering the smallest period) is equal to: 0.2 for the PET, 1.4 for the Ny and 10.6 for the EVA. This implies that plastic elements are immersed (totally or partially) in the boundary layer where the Longuet-Higgins streaming is generated. For this reason, the plastic particle velocity is expected to be driven by that of water, and, in turn, the plastic debris displacement could be easily correlated to that of water particles. However, as will be demonstrated later, the plastic motion is influenced not only by the characteristics of the waves but also by the roughness and slope of the bed and the properties of the plastic samples.
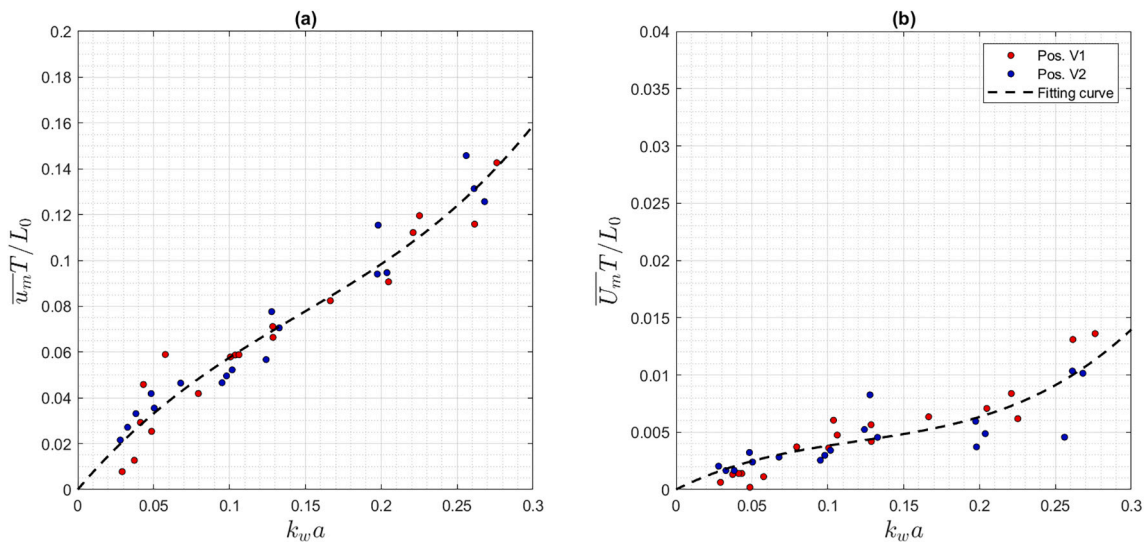

Fig. 4. Velocity close to the bottom ($z < 5$ mm): a) dimensionless maximum values of the phase-average velocity profile for the rough bed case ($\overline{u_m}$), made dimensionless through the wave celerity; b) dimensionless maximum values of the average velocity ($\overline{U_m}$) estimated below $z/\delta < 10$. $\overline{u_m}$ and $\overline{U_m}$ were obtained from the data measured at the position V1 and V2.

Table 4

Characterization of the plastic particles: id indicates the sample name, d_D is the equivalent diameter of a sphere with the same settling velocity, d_p is the characteristic length estimated according to Goral et al. (Goral et al., 2023a), w_s is the measured settling velocity, C_D is the drag coefficient and Re_p is the Reynolds number.

Material	Id	shape	d_D [mm]	d_p [mm]	w_s [cm/s]	C_D [−]	Re_p [−]
PET	PET-01	Rectangular prism	0.18	7.24	2.86	1.07	208.80
PET	PET-02	Square plate	0.18	5.00	2.95	1.01	147.60
Nylon	Ny-01	Rectangular prism	1.20	7.25	4.19	1.31	303.90
Nylon	Ny-02	Square plate	1.20	5.00	4.67	1.05	234.50
EVA	EVA-01	Circular cylinder	7.07	9.22	3.51	0.74	323.70
EVA	EVA-02	Circular cylinder	7.07	7.20	3.48	0.75	251.80
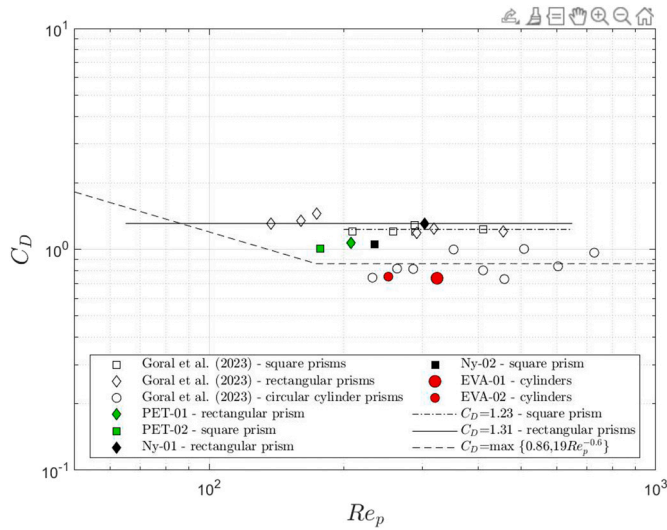
Fig. 5. Comparison between the values of the C_D estimated in the present experimental campaign, the values estimated by Goral et al. (Goral et al., 2023a) and the relationship proposed by Goral et al. (Goral et al., 2023a).

3.2. Settling velocity

The settling velocity is a quantity used for the plastic characterization. It depends on several parameters, the most significant are the density, size and shape of plastic debris and the density and dynamic viscosity of the fluid.

Recently, Goral et al. (Goral et al., 2023a) proposed new formulae which provide an accurate estimate of the drag coefficient for different types of plastic. For each studied shape, the authors individuate a specific relationship which connected the characteristics of the plastic with those of the fluid. In particular, such relationships relate the drag coefficient (C_D) to the Reynolds number of the plastic (Re_p). Considering the reliability of the proposed methods by Goral et al. (Goral et al., 2023a), such relationships were considered as comparison data in the following analysis. When the particle is affected only by the buoyancy force and the drag force, the drag coefficient C_D is equal to:

$$C_D = \frac{4g(s-1)d_D}{2w_s^2} \tag{5}$$

where g is the gravity acceleration, s is the relative density of the plastic (ρ_s) with respect to water density (ρ_s), d_D is the equivalent diameter of a sphere with the same settling velocity, w_s is the settling velocity of the plastic particle. The particle Reynolds number is defined as:

$$Re_p = \frac{w_s d_p}{\nu} \tag{6}$$

where d_p is the characteristic length estimated according to Goral et al. (Goral et al., 2023a). Table 4 shows the characteristics of the samples estimated to evaluate the drag coefficient and the Reynolds number.

According to Goral et al. (Goral et al., 2023a), C_D assumes a constant value equal to 1.23 and 1.31 for square plate shape and rectangular prism shape, respectively. For the cylinder shape, C_D is equal to the maximum value between 0.86 and $19Re_p^{-0.6}$. Fig. 5 shows the comparison between the drag coefficients estimated in the present study and those estimated by Goral et al. (Goral et al., 2023a). The plot also shows the fitting curve of the experimental data proposed by Goral et al. (Goral et al., 2023a).

Generally, the estimated C_D agrees with the values estimated by Goral et al. (Goral et al., 2023a). The relative error is equal to 28 % for the PET-01, 26 % for the PET-02, 0.23 % for the Ny-01, 14 % for the Ny-02, 13 % for the EVA-01, and 14 % for the EVA-01.

From the analysis of the results, it is observed that: i) Ny-01 presents the greatest resistance to flow compared to the other particles; ii) EVA-01 and EVA-02 present the lowest values; iii) the other particles show almost similar values. As will be demonstrated later, the drag coefficient C_D can be used to understand how the wave-driven motion of the plastic particles can be affected by the bed roughness. Indeed, lift forces can be established on plastic particles during the action of waves. As well, as the coefficient of resistance to vertical motion, C_D, increases, it is expected that the particles will be less subject to these fluctuation forces.

3.3. Analysis of plastic debris motion

Plastic particles are initially mobilized by waves and undergo a diffusion process. Subsequently, the transport process initiates with a velocity correlated to the wave characteristics. In particular, in the present experiments, these three types of motion can be identified: zero net transport (motion type 1); transport up to a specific position (motion type 2); and transport up to the breaking zone (motion type 3). An example of type 2 motion has already been shown in Fig. 2. As will be demonstrated later, the type of motion depends on the characteristics of waves and plastics. An example of three types of motion detected during the experimental campaign is shown in Fig. 6.

To compare the dynamics of the various plastic samples, five areas were identified along the beach profile (refer to Fig. 7). Point b indicates the transition between part A and part B (see Fig. 1). Point d represents the depth at which the motion of the plastic sample starts to be affected by the wave breaking. Additionally, for the sake of completeness, two other zones were considered, namely 1 and 3, representing half of the previously described areas.

The average slope angle is approximately equal to 2° and 7.82° for Zone 1 and Zone 2 respectively. Zones 3–4-5 are characterised by a constant slope angle equal to 11.31°.

For the comparative analysis, for each test, the position of the global centroid weighted as a function of the residence time was estimated:

$$X'_g = \frac{\sum_{i=1}^{n_z} X_{g,i} t_i}{\sum_{i=1}^{n_z} t_i} \tag{7}$$

where n_z is the number of zones, t_i is the residence time of the centroid within i-th zone and $X_{g,i}$ is the average position of the centroid in the i-th zone. X'_g was made dimensionless by the wavelength L_0.

Fig. 8 and Fig. 9 show X'_g/L_0 as a function of $k_0 a$ for the smooth and the rough bed respectively. Subplots (a) to (c) are referred to plastics
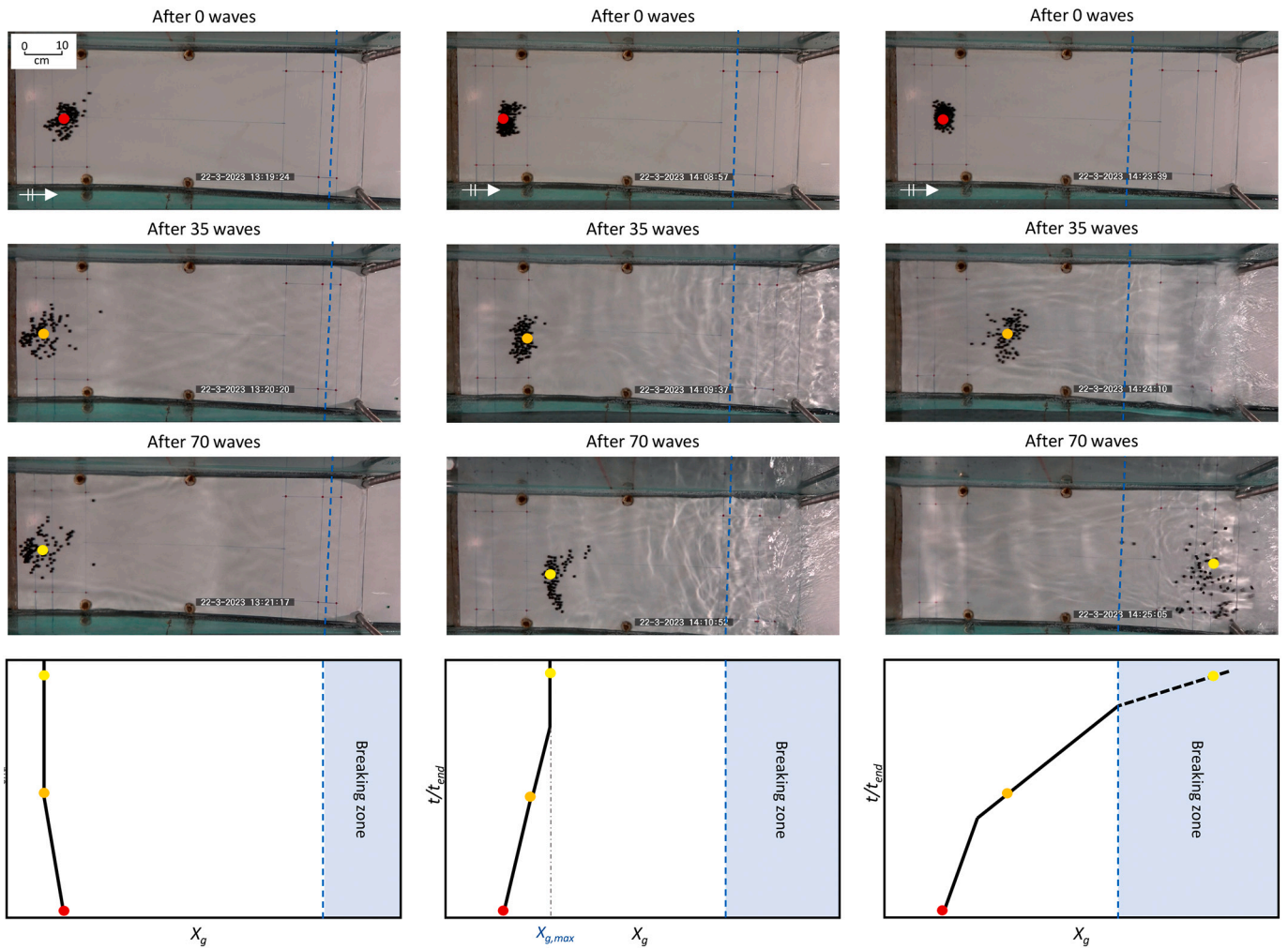
Fig. 6. Three examples of plastic debris transport due to waves. First column: type 1; second column: type 2; third column: type 3. The frames show the elements at the initial position (first row) and after the passage 35 (second row) and 70 waves (third row). The arrow on the bottom left corner indicates the direction of the wave propagation. The point on the frame indicates the position of the centroid, also reported on the sketch in the last row, which mimics the centroid displacement during the test, qualitatively described within the breaking zone (dotted line) since it could not be estimated using blob analysis. The hydrodynamics conditions are: column 1 - H=1.5 cm, T=1.67 s and h=23 cm; column 2 - H=4.4 cm, T=1.25 s and h=18 cm; column 3 - H=8.4 cm, T=1.00 s and h=18 cm.
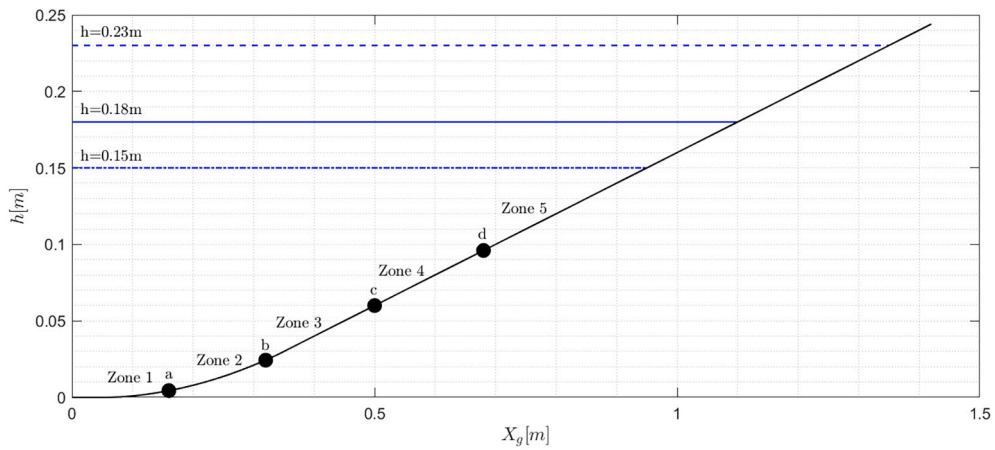
Fig. 7. Beach profile used in the experimental camping. The location of the five zones was identified for the comparison of the dynamics of the different plastic samples. The three blue lines indicate the water levels used during the experiments. (For interpretation of the references to colour in this figure legend, the reader is referred to the web version of this article.)
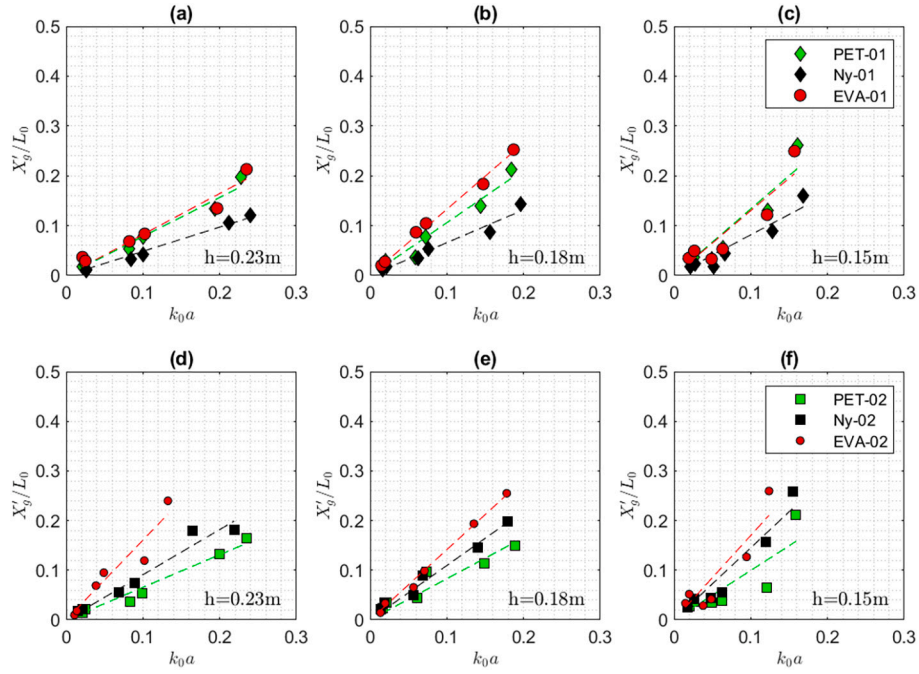
Fig. 8. X_g'/L_0 as a function of k_0a for the smooth bed. The samples were sorted according to their size and the water depth used during the tests.
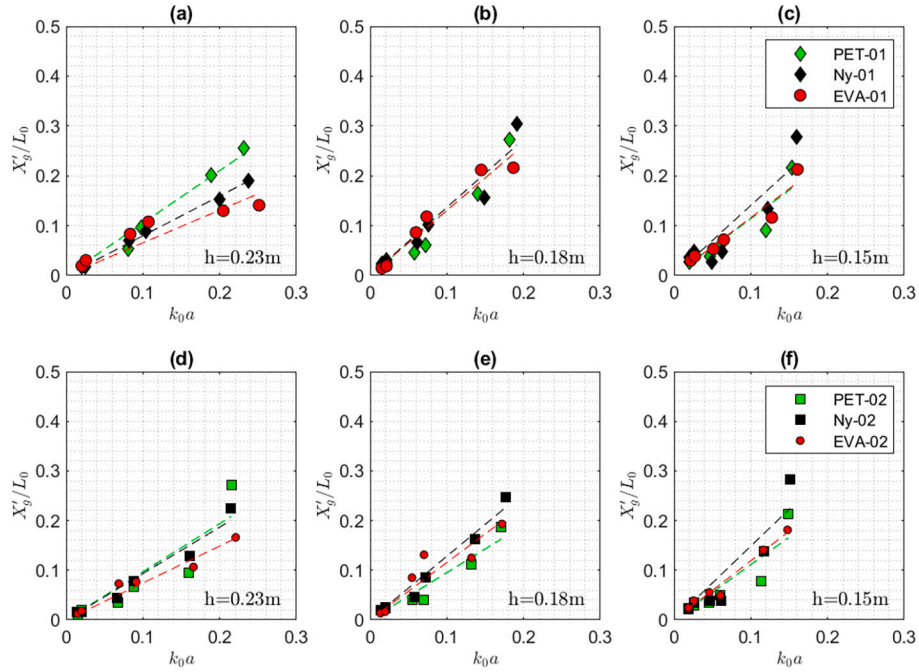

Fig. 9. X_g'/L_0 as a function of k_0a for the rough bed. The samples were sorted according to their size and the water depth used during the tests.

with larger dimensions (PET-01, Ny-01 and EVA-01), while subplots (d) to (f) are for plastics with smaller dimensions (PET-02, Ny-02 and EVA-03). The plastics were sorted according to the three water depths used during the tests.

Fig. 10 shows the slope of the fitting curve estimated for each plastic debris and each water depth. The data points shown in Fig. 8 and Fig. 9 were fitted with a first-degree polynomial of the type: $X_g'/L_0 = P_p k_0 a$. The slope P_p provides a measure of the propensity of the particles to drift: high values indicate low resistance of the particles to wave generated motion.

The bar plot in Fig. 10 allows for a concise analysis of the impact of various factors characterizing the present study. Specifically, it enables the assessment of the effect of the: average water depth, plastic type, plastic size, and seabed type. The comparison between the values of P_p was quantified by means of the parameters $\Delta P_{p,size}$ and $\Delta P_{p,bed}$. For example, for the plastic EVA they were estimated with the following relationship:

$$\Delta P_{p,size} = \frac{\overline{P}_{p,EVA-1} - \overline{P}_{p,EVA-2}}{\overline{P}_{p,EVA-1}} 100 \tag{8}$$
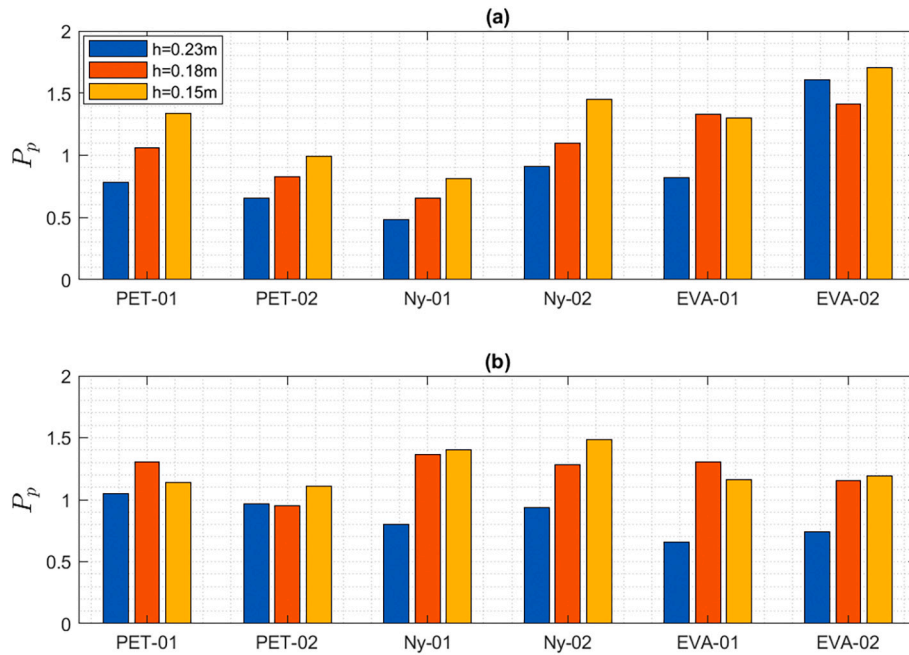
Fig. 10. P_p provides a measure of the propensity of the particles to drift on the smooth surface (a) and rough surface (b): high values indicate low resistance of the particles to motion to the current generated by waves.

Table 5

$\Delta P_{p,size}$ and $\Delta P_{p,bed}$ estimated for the samples. Negative value of $\Delta P_{p,size}$ indicates more resistance of the larger size particles than the smaller size particles. Negative value of $\Delta P_{p,bed}$ indicates more resistance of the particles on the smooth bed than rough bed. Values close to zero indicate similar behaviour between the compared configurations.

Material	$\Delta P_{p,size}$		$\Delta P_{p,bed}$	
	Smooth bed	Rough bed	Larger size	Smaller size
PET	21.13	12.54	−14.36	−24.72
NY	−77.18	−5.49	−81.33	−7.31
EVA	−44.14	−1.50	10.95	34.01

$$\Delta P_{p,bed} = \frac{\overline{P}_{p,EVA-1,smooth} - \overline{P}_{p,EVA-1,rough}}{\overline{P}_{p,EVA-1,smooth}} 100 \qquad (9)$$

where $\overline{P_p}$ indicates the averaged value of P_p for different water depths.

In general, it can be observed that the reduction in particle displacement occurs due to: i) a decrease in wave steepness; ii) an increase in depth; iii) an increase in particle size; iv) an increase in plastic density.

From Figs. 8 and 9 we can see that for all the samples, as the steepness of the wave (expressed as ka) increases, there is a considerable transport of the particles which reach areas with higher slopes. Furthermore, this tendency is highlighted as the water depth decreases. As observed in Section 3.1 for the mass-transport, this behaviour is due to the increase in wave asymmetry, which leads to an increase in the difference between the positive and negative wave phases.

As expected, in the case of Nylon and EVA, the transport tends to decrease as the size of the particle increases (negative value of $\Delta P_{p,size}$, see Table 5). Conversely, the behaviour is opposite in the case of PET (positive value of $\Delta P_{p,size}$). Such differences can be related to the thickness of PET particles, which makes them more difficult to be transported.

The rough bed causes a reduction of the difference between the samples ($\Delta P_{p,size}$ for smooth bed always greater than $\Delta P_{p,size}$ for rough bed), facilitates transport for some plastics (i.e. Ny-01) and hinders it for others (i.e. EVA-02). In this regard, the comparison between the

displacement of the centroid (X_g) on the two beds can be observed from Fig. 11 considering the samples Ny-01 (a) and EVA-02 (b).

This non-linearity can be related to the analyses on settling velocity. Basically, the different behaviour between the smooth and rough surfaces is linked to the particles' propensity to be subject to lift forces. In the case of material with high resistance to vertical motion (high values of C_D), lift forces have a low impact. This implies that particles, such as those of Ny-01, are affected by the bed roughness during all phases of the wave. Therefore, during the negative phases of the wave, when the velocity is smaller than that of the positive phases, the bottom friction leads to a reduction in the oscillation directed towards offshore. Consequently, at the end of each wave cycle, the positive displacement will be greater in the case of a rough surface (see Fig. 12(a)).

The samples EVA-01 and EVA-02 show transport dynamics strongly conditioned by their low density which tends to make the elements jump and fluctuate, minimizing the contact with the bed. For this plastic, it was observed that contact with the surface occurs above all in the positive oscillation phase, while it is reduced in the negative phase, due to the bouncing of the elements. This means that the effect of the roughness only influences the advancement phase and there is no friction effect in the phase opposite to the wave propagation direction. This aspect is more evident for the smaller sample EVA-02 (see Fig. 12(b)).

Fig. 13(a) illustrates the comparison between the maximum distance covered by the centroid ($X_{g,max}$) on the two beds, normalized by the incident wave height.

Fig. 13(b) shows the ratio between the average $X^*_{g,max}$ estimated for the two beds as a function of the drag coefficient estimated through the settling velocity of the particles. $X^*_{g,max}$ was estimated by averaging the values obtained from all hydrodynamic conditions. An increase in particle resistance to fluctuation leads to an increase in the transport in the case of a rough surface. The relationship between the ratio γ_f and C_D can be expressed through the following equation

$$\gamma_f = \frac{\overline{X^*}_{g,max,smooth}}{\overline{X^*}_{g,max,rough}} = -1.25C_D + 2.32 \qquad (10)$$

The coefficient of determination of Eq. 10 is equal to 0.70.
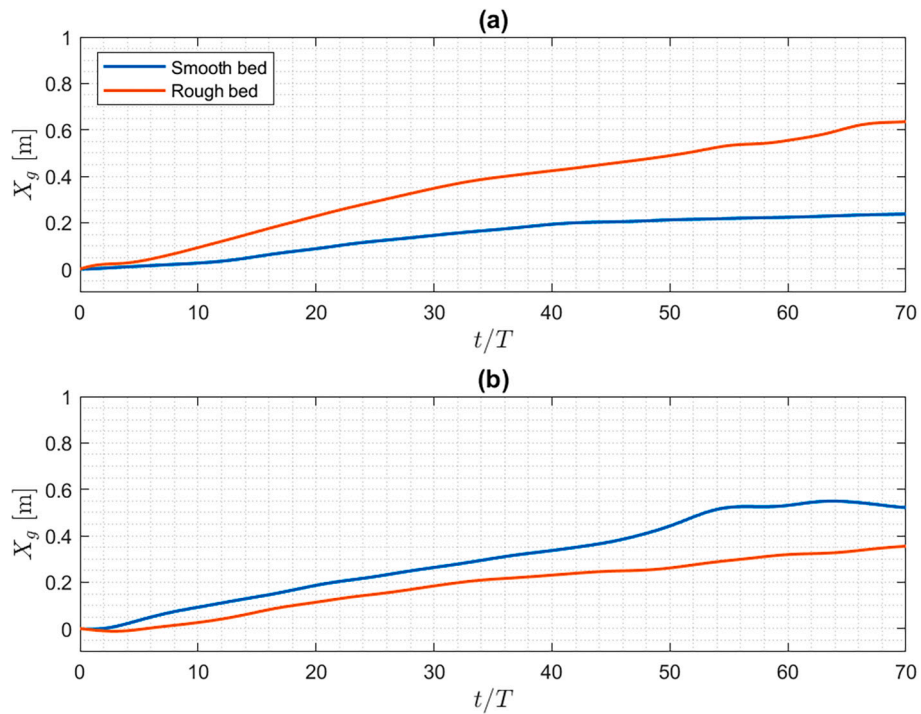
Fig. 11. Differences between the smooth and the rough bed: a) displacement of the sample centroid for the Ny-01; b) displacement of the sample centroid for the EVA-02.
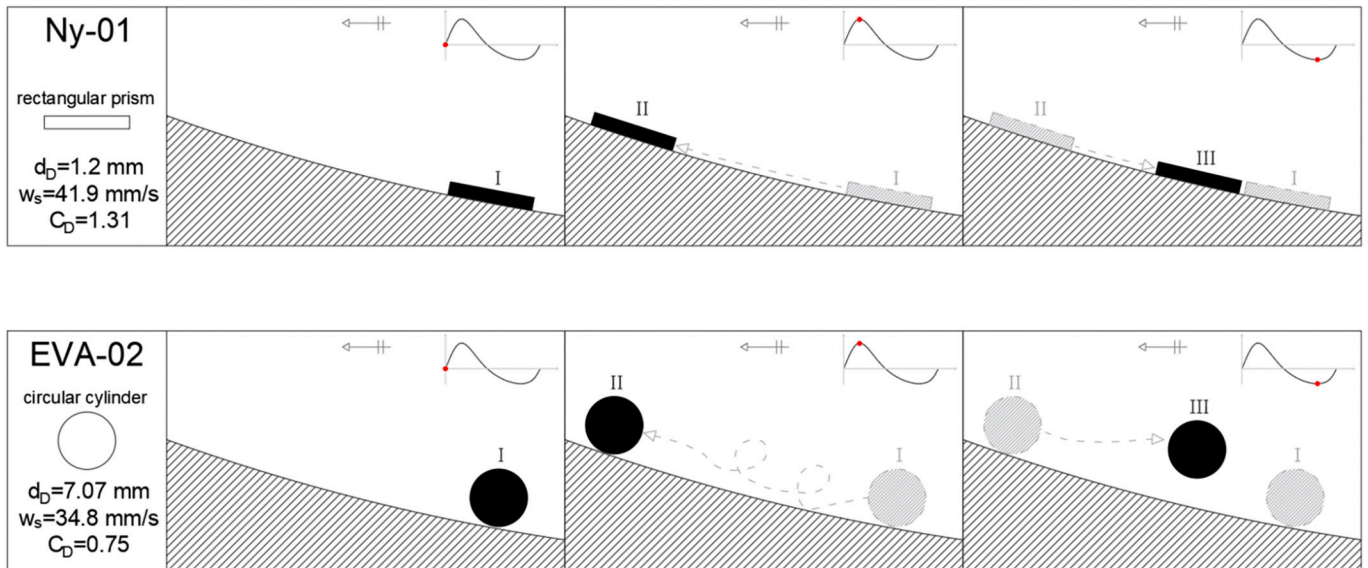

Fig. 12. Schematic illustration of the transport processes during three wave phases: Ny-01 particle at the first row; EVA-02 particle at the second row.

3.4. Criteria for identifying the short-term fate of plastic debris

From the previous analysis, it has been observed that the final position of the sample, i.e. its fate, is influenced by several factors such as the wave characteristics, the water depth, the shape and the density of the plastics and the roughness of the bed. As previously stated, the combination of these characteristics can result in three types of motion. In Type 1 the current generated by the waves cannot move the centroid of the sample. The particles are subjected to an oscillating motion which determines only the expansion of the sample around its centroid. In this case, the drift of the sample is close to zero. In Type 2, the current due to waves mobilizes the particles. Thus, the net drift is greater than zero.

However, for a certain bottom slope, the drift transport vanishes or its velocity becomes very small. When the particle reaches such an equilibrium point, the particles are subjected only to an oscillating motion. In Type 3, the high velocity of the current generated by waves transports the particle to the breaker zone.

The identification of the type of motion represents an important aspect of predicting models of the plastic short-term fate. Once the equilibrium point is reached, $\frac{\Delta X_g}{\Delta t}$ is equal to 0 in motion Type 2. In this case, it is possible to identify a relation between stabilising and destabilising forces. Following a similar approach used in previous studies for oscillatory flow (Shields, 1936; Komar and Miller, 1974), a threshold parameter was defined as a ratio between the hydrodynamic action due
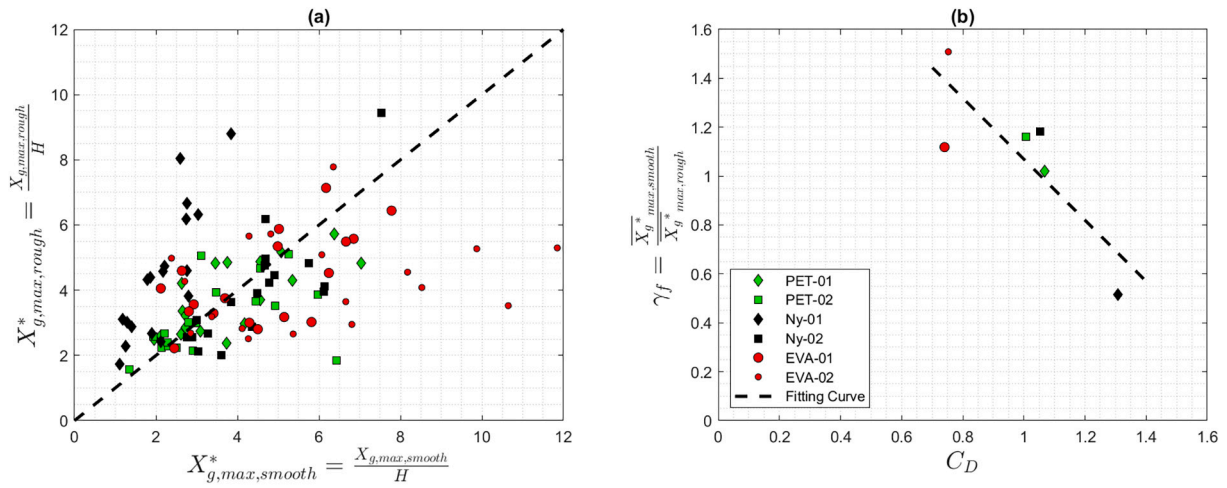
Fig. 13. Differences between the smooth and the rough bed: a) comparison between the maximum distance covered by the centroid $X_{g,max}$ on the two beds made dimensionless with the incident wave height; b) the ratio between the average $X^*_{g,max}$ estimated for the two beds as a function of the drag coefficient estimated through the settling velocity of the particles. $X^*_{g,max}$ for a type of material was estimated by averaging the values obtained from all hydrodynamic conditions.
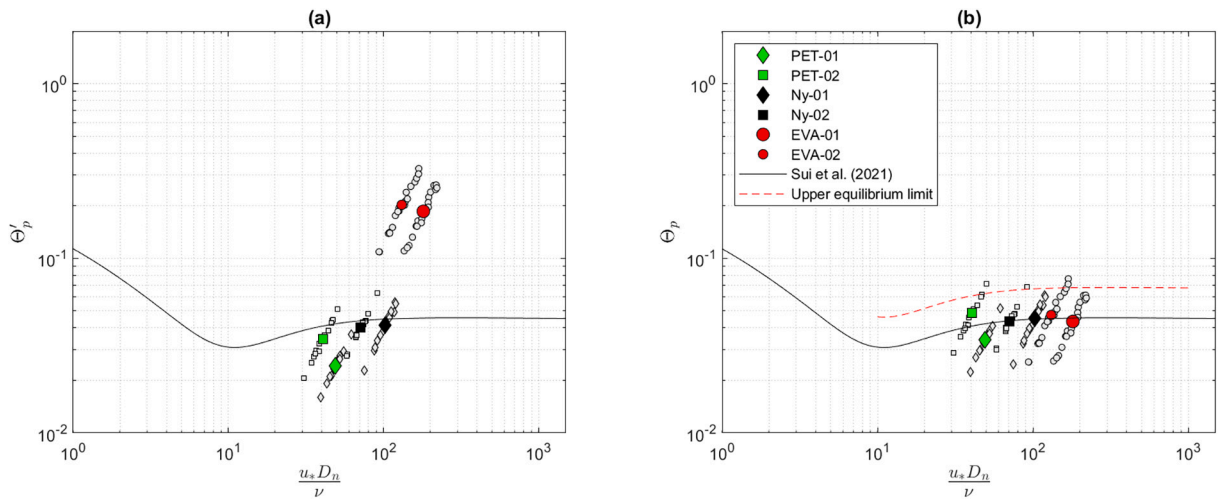

Fig. 14. Threshold parameter: a) Θ'_p as a function of the ratio $\frac{u_* D_n}{\nu}$; b) $\Theta_p = \Theta'_p/\gamma_s$ as a function of the ratio $\frac{u_* D_n}{\nu}$. The two graphs show the approximated Shields curve proposed by Sui et al. (Sui et al., 2021). The grey data points represent the values of hydrodynamic conditions classified as Type 2 for each plastic. The coloured data points represent the mean value of all conditions studied for each plastic.

to waves (F_w), the particle weight (F_p) and the bed slope (F_b). The parameter Θ_S introduced by Shields (Shields, 1936) for a horizontal bed and a uniform grain size is defined as:

$$\Theta_S = \frac{F_w}{F_p F_b} = \frac{u_*^2}{g(s-1)D_n} \tag{11}$$

The Eq. 11 was adapted to take into account the different behaviour of the plastic sample with respect to that of sediment on a horizontal bed:

$$\Theta'_p = \frac{F_w}{F_p F_b} = \frac{u_*^2}{g(s-1)D_n\left(1 + tan\left(\alpha'_{g,max}\right)\right)} \tag{12}$$

where $\alpha'_{g,max}$ is the bed slope, D_n is the diameter of a volume-equivalent sphere (see Table 3) and u_* is the friction velocity estimated according to Komar and Miller (Komar and Miller, 1974) (eq. 19). The prediction capability of a such method is shown in 6. The method of Komar and Miller (Komar and Miller, 1974) was used provided as input the water depth ($h'_{g,max}$), the wave number ($k_{g,max}$), the wave period (T) and incident wave height (H) multiplied with the shoaling coefficient (k_s). k_s was

estimated using the linear theory to take into account the effect of the bed on the wave shape. The quantities $\alpha'_{g,max}$ and $h'_{g,max}$ represent, respectively, the average values of the slope and water depth of the sample centroid in the furthest reached zone. To account for the differences between the two beds, the values of $h_{g,max}$ and $\alpha_{g,max}$ estimated for the rough seabed were multiplied by the coefficient γ_f estimated with Eq. 10. h'_{max} is equal to $\gamma_f h_{g,max}$ with γ_f equal to 1 for the smooth bed or estimated with Eq. 10 for the rough bed. The same procedure was adopted for estimating $\alpha'_{g,max}$.

Fig. 14a) shows Θ'_p as a function of $\frac{u_* D_n}{\nu}$ for the present data along with the Shields curve approximated with the relationship proposed by Sui et al. (Sui et al., 2021). The data display both dispersion around the mean value due to the inherent nonlinearities in the investigated process, and for a fixed sample, an average value that differs from the Shields curve. Regarding the first aspect, theoretically, Θ'_p should be unique for each plastic sample. However, a series of non-linearities intervene causing such dispersion, which is difficult to be predicted. As regards the second aspect, the equilibrium condition requires that the combination of the force which moves the particles in the offshore

direction has to compensate for the displacement reached during the positive phases of waves. In the present experiment, it was observed that for the plastic samples to achieve such conditions is required a value of Θ'_p which differs from the Shields curve (Θ_S) of a quantity function of the plastic density. The weight of the samples causes sliding along the slope. As the weight decreases, its contribution to reaching the equilibrium condition is compensated mainly by the displacement caused by the negative phases of the wave. The term γ_s has been introduced in Eq. 12 to consider such aspect:

$$\Theta_p = \frac{F_w}{F_p F_b} = \frac{u_*^2}{\gamma_s g(s-1)D_n\left(1 + tan\left(\alpha'_{g,max}\right)\right)} \tag{13}$$

It has been observed that the equilibrium condition is reached on average for Θ'_p/Θ_S=0.73, Θ'_p/Θ_S=0.95 and Θ'_p/Θ_S=4.26 for PET, Nylon and EVA respectively. According to such results, the γ_s is defined as

$$\gamma_s = 65.17s^2 - 165.08s + 104.52 \tag{14}$$

Fig. 14b) shows Θ_p estimated with Eq. 13 as a function of $\frac{u_* D_n}{\nu}$.

It must be considered that the conditions of incipient motion and those of stop are closely similar to each other, making it difficult to identify a distinct threshold value. To take this uncertainty into account, Fig. 14b) shows also the upper limit below which the motion of the plastic can be assumed to be close to zero. These limits were identified by shifting the Shields curve to include 95 % of the observed sample. The increase factor for the Sui et al. (Sui et al., 2021) relationship to individuated upper is equal to 1.50.

4. Conclusions

This paper focused on investigating plastic transport in the case of sloping seabeds. It is important to emphasize that while conducted rigorously, the investigations are affected by certain simplifications of reality. These include the lack of morphological bed variations and transverse currents, as well as the use of uniform bed roughness and particle size, the presence of particles on the bed surface rather than buried, regular waves, and freshwater conditions. However, such simplifications are necessary to overcome practical limitations. In this regard, it is recommended to use the results of this study while considering these operational constraints. Despite this complexity reduction, examining different configurations enabled us to understand various aspects of the transport processes. The innovative aspect of this study, compared to previous ones, is the detailed analysis of particle dynamics, including the impact of bed roughness between the shoaling and breaking zones. Indeed, previous studies generally extended the analyses to nearshore regions and over a significantly long time scale (Forsberg et al., 2020; Núñez et al., 2023; Kerpen et al., 2020; Guler et al., 2022). In such studies, the dynamics of the plastic are analysed by comparing the distribution of particles at fixed discrete time steps.

The analysis of plastic sample dynamics carried out in the present work allowed us to identify different types of motion that can occur as well as the effects associated with hydrodynamic conditions, plastic characteristics, and bed features. According to previous studies (Forsberg et al., 2020; Alsina et al., 2020), in the experimental campaign, near the bed, a current is generated that tends to move the water towards the shoreline with a velocity that increases as the steepness of the wave increases. A similar behaviour has been observed for plastics.

Differently from what was observed by Alsina et al. (Alsina et al., 2020), in the present study, it was observed that as the steepness of the wave increases, the displacement of plastics from their initial position also increases.

The distance covered by the particles depends on the bed characteristics and their shape and density. In the case of a rough surface, it has been observed that the differences between various plastics tend to decrease. The roughness of the seabed determines a nonlinear behaviour that is primarily conditioned by the resistance of particles to fluctuation. A greater displacement has been observed on rough surfaces for plastics with high resistance to vertical motion. Conversely, plastics with reduced resistance tend to have longer displacements on smooth surfaces. For a fixed density, particles with larger volumes generally cover shorter distances. However, an opposite trend has been observed in the case of PET.

The analysis of tests where the equilibrium condition is reached allowed for the identification of a criterion to distinguish the types of motion that mobilize the plastic. Adopting the approaches commonly used to identify the conditions of incipient motion of sediments, on average, equilibrium conditions are established when the threshold parameter Θ_p values are close to the Shields curve. The identified method could be implemented in numerical models to simulate the transport of plastics in the coastal areas.

Although an extensive experimental campaign was conducted to describe the motion of plastics on a sloping bed, some questions remain open. In particular, future research activities should be conducted by expanding the types of analysed plastics (shape and density) and varying the characteristics of the seabed (mobile bed, sediment size, slope).

CRediT authorship contribution statement

Claudio Iuppa: Writing – original draft, Writing – review & editing, Visualization, Methodology, Investigation, Data curation, Conceptualization, Funding acquisition. **Giovanni Passalacqua:** Writing – original draft, Software, Methodology, Investigation, Data curation. **Carla Faraci:** Writing – original draft, Writing – review & editing, Supervision, Methodology, Conceptualization, Funding acquisition.

Declaration of competing interest

The authors declare that they have no known competing financial interests or personal relationships that could have appeared to influence the work reported in this paper.

Data availability

Data will be made available on request.

Appendix A. Prediction relationships for maximum values of the phase-average and time-averaged velocity

Two prediction relationships were defined for the maximum values of the phase-average velocity and the maximum values of the time-averaged velocity respectively. As can be seen from Fig. 4, the data collected at the positions V1 and V2 can be fitted with a single curve both for $\frac{\overline{u_m}T}{L_0}$ and $\frac{\overline{U_m}T}{L_0}$. The equations of the fitting curves are:

$$\frac{\overline{u_m}T}{L_0} = 6.06(k_w a)^3 - 2.66(k_w a)^2 + 0.78 k_w a \tag{A.1}$$

$$\frac{\overline{U_m}T}{L_0} = 1.38(k_w a)^3 - 0.48(k_w a)^2 + 0.07 k_w a \tag{A.2}$$

The coefficients of determination of the two relationships are equal to 0.94 and 0.77, respectively.

Appendix B. Methodology adopted to estimate the friction velocity

The quantification of the threshold parameter, introduced in Section 2.4, requires the estimation of a characteristic velocity of water due to wave. In the present study, following the approach adopted by Shields (Shields, 1936), reference was carried out to the friction velocity u_* which is related to the bed shear stress (τ) through $u_* = \sqrt{\tau/\rho_w}$. However, since τ was not directly measured, empirical methods found in the literature were utilized. In particular, Komar and Miller (Komar and Miller, 1974) defined friction velocity as:

$$u_{*K} = \sqrt{\frac{1}{2}f_w}\,u_w \tag{B.1}$$

where u_w is near-bottom velocity and f_w is the friction factor estimated as $f_w = 2RE^{-0.5}$ according to Jonsson (Jonsson, 1966). In the case of oscillating motion, the Reynolds number (RE) is equal to:

$$RE = \frac{u_w A_w}{\nu} \tag{B.2}$$

where A_w is the semi-orbital excursion ($A_w = \frac{u_w T}{2\pi}$). Considering such relationships, Eq. B.1 became:

$$u_{*K} = \left(\left(\frac{2\pi}{T}\right)^{1.5} \sqrt{\nu}\; \frac{(H)}{2\sinh(k_w h_w)} \right)^{0.5} \tag{B.3}$$

Fig. B.15 shows the comparison between u_{*K} and u_{*O} estimated using as input the data of the present experimental campaign. In particular, u_{*O} differs from u_{*K} because u_w was set equal to the near-bottom velocity obtained from the tests ($\overline{u_m}$).
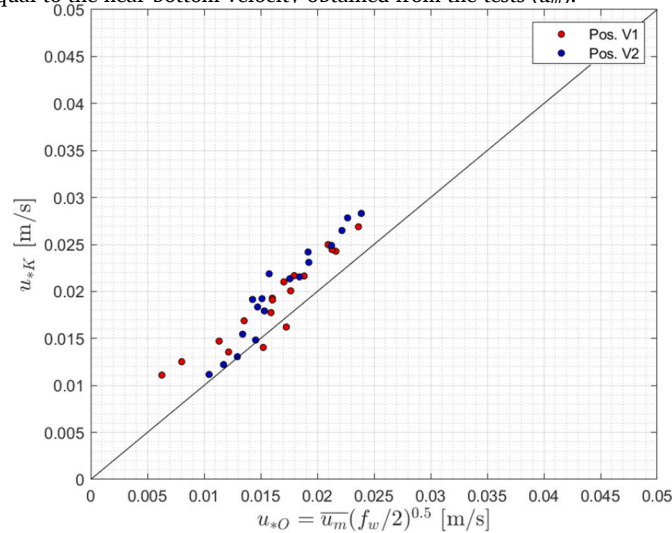

Fig. B.15. Comparison between the friction velocity estimated using $\overline{u_m}$ and f_w and that estimated using the relationship proposed by Komar and Miller (Komar and Miller, 1974).

The root mean square between the two friction velocities is equal to 0.0034 m/s. Given the strong agreement, the method proposed by Komar and Miller (Komar and Miller, 1974) was used to estimate the friction velocity for the tests where velocity data were not available, namely, for the tests where plastics were present.

References

Alsina, J.M., Jongedijk, C.E., van Sebille, E., 2020. Laboratory measurements of the wave-induced motion of plastic particles: Influence of wave period, plastic size and plastic density. J. Geophys. Res. Oceans 125, e2020JC016294.

Collins, J., 1963. Inception of turbulence at the bed under periodic gravity waves. J. Geophys. Res. 68, 6007–6014.

Crawford, C., Quinn, B., 2017. Microplastic Pollutants. Elsevier.

De-la Torre, G.E., Dioses-Salinas, D.C., Castro, J.M., Antay, R., Fernández, N.Y., Espinoza-Morriberón, D., Saldaña-Serrano, M., 2020. Abundance and distribution of microplastics on sandy beaches of lima, peru. Mar. Pollut. Bull. 151, 110877.

Elisei Schicchi, A., Moreira, D., Eisenberg, P., Simionato, C.G., 2023. Qualitative study of the transport of microplastics in the río de la plata estuary, argentina, through numerical simulation. Journal of Marine Science and Engineering 11, 2317.

Faraci, C., Musumeci, R., Marino, M., Ruggeri, A., Carlo, C., Jensen, B., Foti, E., Barbaro, G., Elsaber, B., 2021. Wave- and current-dominated combined orthogonal flows over fixed rough beds. Cont. Shelf Res. 220, 104403.

Forsberg, P.L., Sous, D., Stocchino, A., Chemin, R., 2020. Behaviour of plastic litter in nearshore waters: First insights from wind and wave laboratory experiments. Mar. Pollut. Bull. 153, 111023.

Francalanci, S., Paris, E., Solari, L., 2021. On the prediction of settling velocity for plastic particles of different shapes. Environ. Pollut. 290, 118068.

Fredsoe, J., Deigaard, R., 1992. Mechanics of Coastal Sediment Transport, 3. World Scientific Publishing Company.

Goral, K.D., Guler, H.G., Larsen, B.E., Carstensen, S., Christensen, E.D., Kerpen, N.B., Schlurmann, T., Fuhrman, D.R., 2023a. Settling velocity of microplastic particles having regular and irregular shapes. Environ. Res. 228, 115783.

Goral, K.D., Guler, H.G., Larsen, B.E., Carstensen, S., Christensen, E.D., Kerpen, N.B., Schlurmann, T., Fuhrman, D.R., 2023b. Shields diagram and the incipient motion of microplastic particles. Environ. Sci. Technol. 57, 9362–9375.

Guerrini, F., Mari, L., Casagrandi, R., 2021. The dynamics of microplastics and associated contaminants: data-driven Lagrangian and eulerian modelling approaches in the mediterranean sea. Sci. Total Environ. 777, 145944. URL: https://www.sciencedirect.com/science/article/pii/S0048969721010111 https://doi.org/10.1016/j.scitotenv.2021.145944.

Guler, H.G., Larsen, B.E., Quintana, O., Goral, K.D., Carstensen, S., Christensen, E.D., Kerpen, N.B., Schlurmann, T., Fuhrman, D.R., 2022. Experimental study of non-buoyant microplastic transport beneath breaking irregular waves on a live sediment bed. Mar. Pollut. Bull. 181, 113902.

Hardesty, B., Harari, J., Isobe, A., Lebreton, L., Maximenko, N., Potemra, J., van Sebille, E., Vethaak, A., Wilcox, C., 2017. Using numerical model simulations to improve the understanding of micro-plastic distribution and pathways in the marine environment. Front. Mar. Sci. 4.

Jalón-Rojas, I., Wang, X.H., Fredj, E., 2019. A 3d numerical model to track marine plastic debris (trackmpd): Sensitivity of microplastic trajectories and fates to particle dynamical properties and physical processes. Mar. Pollut. Bull. 141, 256–272. URL: https://www.sciencedirect.com/science/article/pii/S0025326X19301523 https://doi.org/10.1016/j.marpolbul.2019.02.052.

Jonsson, I.G., 1966. Wave boundary layers and friction factors. In: Coastal Engineering, 1967, pp. 127–148.

Kerpen, N.B., Schlurmann, T., Schendel, A., Gundlach, J., Marquard, D., Hüpgen, M., 2020. Wave-induced distribution of microplastic in the surf zone. Front. Mar. Sci. 7, 590565.

Komar, P.D., Miller, M.C., 1974. Sediment threshold under oscillatory waves. Coast. Eng. 1975, 756–775.

Larsen, B.E., Al-Obaidi, M.A.A., Guler, H.G., Carstensen, S., Goral, K.D., Christensen, E. D., Kerpen, N.B., Schlurmann, T., Fuhrman, D.R., 2023. Experimental investigation on the nearshore transport of buoyant microplastic particles. Mar. Pollut. Bull. 187, 114610. URL: https://www.sciencedirect.com/science/article/pii/S0025326X23000413 https://doi.org/10.1016/j.marpolbul.2023.114610.

Lebreton, L.-M., Greer, S., Borrero, J., 2012. Numerical modelling of floating debris in the world's oceans. Mar. Pollut. Bull. 64, 653–661. URL: https://www.sciencedirect.com/science/article/pii/S0025326X11005674 https://doi.org/10.1016/j.marpolbul.2011.10.027.

Li, Y., Xiao, P., Donnici, S., Cheng, J., Tang, C., 2023. Spatial and seasonal distribution of microplastics in various environmental compartments around sishili bay of north yellow sea, china. Mar. Pollut. Bull. 186, 114372.

Liao, F., Wang, X.H., Fredj, E., 2023. Forecasting marine debris spill accumulation patterns in the south-eastern australia water: an intercomparison between global ocean forecast models. Ocean Dyn. 73, 91–106.

Liubartseva, S., Coppini, G., Lecci, R., Clementi, E., 2018. Tracking plastics in the mediterranean: 2d lagrangian model. Mar. Pollut. Bull. 129, 151–162. URL: https://www.sciencedirect.com/science/article/pii/S0025326X18301000 https://doi.org/10.1016/j.marpolbul.2018.02.019.

Longuet-Higgins, M.S., 1953. Mass transport in water waves. Philosophical Transactions of the Royal Society of London. Series A, Mathematical and Physical Sciences 245, 535–581.

Mansard, E.P., Funke, E., 1980. The measurement of incident and reflected spectra using a least squares method, in. Coast. Eng. 154–172.

Moeslund, T.B., 2012. Introduction to Video and Image Processing: Building Real Systems and Applications. Springer Science & Business Media.

Núñez, P., Romano, A., García-Alba, J., Besio, G., Medina, R., 2023. Wave-induced cross-shore distribution of different densities, shapes, and sizes of plastic debris in coastal environments: a laboratory experiment. Mar. Pollut. Bull. 187, 114561.

Passalacqua, G., Iuppa, C., Faraci, C., 2023. A simplified experimental method to estimate the transport of non-buoyant plastic particles due to waves by 2d image processing. Journal of Marine Science and Engineering 11. URL: https://www.mdpi.com/2077-1312/11/8/1599 https://doi.org/10.3390/jmse11081599.

Pilechi, A., Mohammadian, A., Murphy, E., 2022. A numerical framework for modeling fate and transport of microplastics in inland and coastal waters. Mar. Pollut. Bull. 184, 114119.

Riley, N., 2001. Steady streaming. Annu. Rev. Fluid Mech. 33, 43–65.

Scandura, P., Foti, E., Faraci, C., 2012. Mass transport under standing waves over a sloping beach. J. Fluid Mech. 701, 460–472.

Shields, A., 1936. Anwendung der aehnlichkeitsmechanik und der turbulenzforschung auf die geschiebebewegung. PhD Thesis. Technical University, Berlin.

Stagnitti, M., Musumeci, R., 2024. Model-based estimation of seasonal transport of macro-plastics in a marine protected area. Mar. Pollut. Bull. 201, 116191.

Stokes, G.G., 1847. On the theory of oscillatory waves. Trans. Cam. Philos. Soc. 8, 441–455.

Sui, T., Staunstrup, L.H., Carstensen, S., Fuhrman, D.R., 2021. Span shoulder migration in three-dimensional current-induced scour beneath submerged pipelines. Coast. Eng. 164, 103776.

Thomas, R., Schindfessel, L., McLelland, S., Creëlle, S., De Mulder, T., 2017. Bias in mean velocities and noise in variances and covariances measured using a multistatic acoustic profiler: the nortek vectrino profiler. Meas. Sci. Technol. 28, 075302.

Uzun, P., Farazande, S., Guven, B., 2022. Mathematical modeling of microplastic abundance, distribution, and transport in water environments: a review. Chemosphere 288, 132517.

Van Sebille, E., Aliani, S., Law, K.L., Maximenko, N., Alsina, J.M., Bagaev, A., Bergmann, M., Chapron, B., Chubarenko, I., Cózar, A., et al., 2020. The physical oceanography of the transport of floating marine debris. Environ. Res. Lett. 15, 023003.

Waldschläger, K., Schüttrumpf, H., 2019. Erosion behavior of different microplastic particles in comparison to natural sediments. Environ. Sci. Technol. 53, 13219–13227.

Yu, Z., Yang, G., Zhang, W., 2022. A new model for the terminal settling velocity of microplastics. Mar. Pollut. Bull. 176, 113449.